



Significance of the spectral correction of photon counting detector response in material classification from spectral x-ray CT

Jumanazarov, Doniyor; Koo, Jakeoung; Poulsen, Henning F.; Olsen, Ulrik L.; Iovea, Mihai

Published in:
Journal of Medical Imaging

Link to article, DOI:
[10.1117/1.JMI.9.3.034504](https://doi.org/10.1117/1.JMI.9.3.034504)

Publication date:
2022

Document Version
Publisher's PDF, also known as Version of record

[Link back to DTU Orbit](#)

Citation (APA):
Jumanazarov, D., Koo, J., Poulsen, H. F., Olsen, U. L., & Iovea, M. (2022). Significance of the spectral correction of photon counting detector response in material classification from spectral x-ray CT. *Journal of Medical Imaging*, 9(3), Article 034504. <https://doi.org/10.1117/1.JMI.9.3.034504>

General rights

Copyright and moral rights for the publications made accessible in the public portal are retained by the authors and/or other copyright owners and it is a condition of accessing publications that users recognise and abide by the legal requirements associated with these rights.

- Users may download and print one copy of any publication from the public portal for the purpose of private study or research.
- You may not further distribute the material or use it for any profit-making activity or commercial gain
- You may freely distribute the URL identifying the publication in the public portal

If you believe that this document breaches copyright please contact us providing details, and we will remove access to the work immediately and investigate your claim.

Significance of the spectral correction of photon counting detector response in material classification from spectral x-ray CT

Doniyor Jumanazarov,^{a,b,*} Jakeoung Koo^{b,c}, Henning F. Poulsen^{b,a},
Ulrik L. Olsen,^a and Mihai Iovea^b

^aTechnical University of Denmark, DTU Physics, Lyngby, Denmark

^bACCENT PRO 2000 s.r.l. (AP2K), Bucharest, Romania

^cTechnical University of Denmark, DTU Compute, Lyngby, Denmark

Abstract

Purpose: Photon counting imaging detectors (PCD) has paved the way for spectral x-ray computed tomography (spectral CT), which simultaneously measures a sample's linear attenuation coefficient (LAC) at multiple energies. However, cadmium telluride (CdTe)-based PCDs working under high flux suffer from detector effects, such as charge sharing and photon pileup. These effects result in the severe spectral distortions of the measured spectra and significant deviation of the extracted LACs from the reference attenuation curve. We analyze the influence of the spectral distortion correction on material classification performance.

Approach: We employ a spectral correction algorithm to reduce the primary spectral distortions. We use a method for material classification that measures system-independent material properties, such as electron density, ρ_e , and effective atomic number, Z_{eff} . These parameters are extracted from the LACs using attenuation decomposition and are independent of the scanner specification. The classification performance with the raw and corrected data is tested on different numbers of energy bins and projections and different radiation dose levels. We use experimental data with a broad range of materials in the range of $6 \leq Z_{\text{eff}} \leq 15$, acquired with a custom laboratory instrument for spectral CT.

Results: We show that using the spectral correction leads to an accuracy increase of 1.6 and 3.8 times in estimating ρ_e and Z_{eff} , respectively, when the image reconstruction is performed from only 12 projections and the 15 energy bins approach is used.

Conclusions: The correction algorithm accurately reconstructs the measured attenuation curve and thus gives better classification performance.

© 2022 Society of Photo-Optical Instrumentation Engineers (SPIE) [DOI: [10.1117/1.JMI.9.3.034504](https://doi.org/10.1117/1.JMI.9.3.034504)]

Keywords: spectral x-ray CT; material classification; photon counting x-ray detector; joint reconstruction; medical applications; low dose imaging.

Paper 21176RR received Jul. 9, 2021; accepted for publication Jun. 16, 2022; published online Jun. 30, 2022.

1 Introduction

Conventional x-ray computed tomography (CT) reconstructs a structural image of the distribution of the averaged linear attenuation coefficients (LAC) within the scanned object. This is because the polychromatic nature of the incoming x-ray photons is disregarded. The averaged LAC reports the quantity of radiation attenuated by a material and integrated over the wide energy range between 20 and 160 keV. A polychromatic beam is generated by a tungsten laboratory x-ray source. The difference of the averaged LAC between different objects gives the contrast that enables material classification in, e.g., medical diagnosis. However, the averaged LACs for some materials of different chemical compositions may be overlapping, which

*Address all correspondence to Doniyor Jumanazarov, doniyor.jumanazarov@fysik.dtu.dk

significantly restricts the classification performance from single energy CT data. The main reasons are that the energy dependence of the attenuation is not measured, and the LAC is dependent on material properties, such as electron density, ρ_e , and effective atomic number, Z_{eff} . Different human tissues may possess overlapping attenuation properties, in spite of having different ρ_e or Z_{eff} , which leads to low contrast of soft tissues in CT.¹⁻³ This suggests a requirement for resolving the x-ray spectrum into multiple energy bins, which enables decomposition of LAC into ρ_e and Z_{eff} . Quantitative characterization based on the distribution of ρ_e and Z_{eff} within the object is a very useful technique in radiotherapy and medical diagnosis applications⁴⁻⁸ and explosive detection.⁹

Alvarez and Macovski¹⁰ proposed an alternative method that decomposes a material's LAC into photoelectric absorption and Compton scattering cross sections and can define the whole spectral range of the LAC through just two parameters, density, ρ , and effective atom number, Z_{eff} . This laid the foundation for dual-energy CT, which can extract the LAC at low and high energies, and reconstruct a map of both ρ_e and Z_{eff} . This system is currently used for material recognition with two channels of energy discrimination in medical and security applications.^{3,11-19} Dual-energy CT is performed in two ways, either by switching the accelerating voltage of the source and making two consecutive measurements with a traditional energy integrating detector at both high and low bias or using a sandwiched detector that simultaneously measures a low energy spectrum with the first thin layer and the remaining high energy spectrum with the second thicker layer.²⁰ The dual-energy CT systems suffer from two main limitations. First, low and high energies are overlapping, leading to low energy separation. Second, this system only measures two different data points in the attenuation spectrum and therefore provides limited material classification maps. Furthermore, material identification through the averaged LAC computed from overlapping energies is a system-dependent solution, i.e., it depends on source spectrum, filtration, and detector efficiency of the scanner.²¹

The development of cadmium telluride (CdTe) energy discriminating imaging detectors has laid groundbreaking step toward multienergy spectral CT.^{22,23} Energy-resolved photon counting detectors (PCD) can discriminate the energy of the incident photons and enable the simultaneous collection of the full spectrum of material's energy-dependent LACs. Spectral CT simultaneously measures the energy dependence of a material's LAC using a PCD and is proved to present significantly greater potential to enhance material classification compared to dual-energy CT.²⁴ Therefore, spectral CT has attracted a large interest within medical²⁵⁻²⁹ and security applications.^{30,31} Recent developments in spectral CT for clinical applications have been reported in the literature,³²⁻³⁶ which include enhanced image resolution, decreased metal, and beam-hardening artifacts, and the ability to reduce radiation dose and differentiate among various contrast materials. Lung nodules, implants such as stents, and small bone parts or small blood vessels can be visualized with enhanced spatial resolution using PCDs.³⁷⁻⁴¹ Radiography studies in security screening also showed that PCDs have clear advantages over dual-layer sandwich detectors in improving material recognition.⁴²⁻⁴⁵ The poor spectral separation in the dual-layer sandwich detectors was found to be the major reason for the lower performance.

Azevedo et al.⁴⁶ recently presented a method that measures (ρ_e , Z_{eff}) from dual-energy CT called the system-independent ρ_e/Z_{eff} (SIRZ), independent of the scanning instrument, and Champley et al.⁴⁷ improved the method further (SIRZ-2). Busi et al.⁴⁸ adopted the SIRZ method for spectral CT with the spectral ρ_e/Z_{eff} estimation (SRZE) method, which measures both system-independent material features directly from the spectral LACs. However, the SRZE method uses 64 energy bins for the optimal accuracy and gives significantly lower accuracy with two energy bins.

In previous work, we presented a classification method, named system-independent material classification through attenuation decomposition (SIMCAD),⁴⁹ which measures the material features (ρ_e , Z_{eff}), independent of the instrument or specifics of the scanner such as x-ray spectrum, directly from energy-resolved LACs in spectral CT. The method uses attenuation decomposition presented by Alvarez and Macovski¹⁰ for the formulation and adopts it for multiple energies. It was demonstrated with the experimental data that the SIMCAD method can reach the optimal classification performance with optimized bienergy bins and can give the results comparable to the SRZE method. Therefore, the SIMCAD method spends at least 32× shorter time for the

tomographic reconstruction after the data acquisition due to a lower number of energy bins used. The speed makes the method well suited for applications where rapid scanning is required.

The above classification methods rely on accurate LAC curves. However, detector effects, such as charge sharing and weighting potential (WP) cross-talk, x-ray fluorescence radiation, Compton scattering, pulse pile up, and incomplete charge collection (ICC), strongly distort the measured spectrum of photon-counting x-ray detectors operating under high flux.²⁶ These effects lead to severe deviation between the measured and transmitted spectrum, and therefore to a significant decrease in material identification performance. Thus, the correction of the detector's spectral response is required to correct the measured LACs. To correct for these distortions, we use a correction algorithm developed by Dreier et al.⁵⁰ This is a comprehensive semianalytical correction algorithm that corrects the raw data distorted by the detector effects based on spectral distortion models. With small adjustments, the correction algorithm could be applied to any photon counting CdTe detector.

In this work, we analyze the contribution of the correction algorithm in material classification from spectral CT measurements, since the spectral correction requires additional computation time valuable in real applications. We use an L_∞ norm-based vectorial total variation (L_∞ -VTV) for image reconstructions from the spectral sinograms. This joint reconstruction algorithm uses an L_∞ norm that jointly penalizes the violation of the inter energy bin dependency, resulting in strong coupling among energy bins. The image reconstruction quality is evaluated with the correlation coefficient that is computed relative to ground-truth images. The material classification performance both for raw and corrected data is tested on "real life" phantoms using real experimental data. We use 20 different materials for calibrating the classification method and 15 additional materials for evaluating the classification performance in the range of $6 \leq Z_{\text{eff}} \leq 15$. The classification performance for the raw and corrected data is performed with respect to different numbers of energy bins and projections and different integration times of the PCD used.

2 Experimental Setup and Materials: Data Correction Algorithm

In this section, we define the system-independent physical properties used to classify materials and LACs. We then present the experimental setup and the samples used to conduct the experiments. Lastly, the detector, data correction, and sinogram generation are introduced.

2.1 Physical Properties of Materials

LAC is proportionally dependent upon a material's electron density.⁵¹ The electron density is the number of electrons per unit volume (electron – mole/cm³). For a compound or mixture that consists of N total different elements, the electron density can be expressed as

$$\rho_e = \frac{\sum_{i=1}^N \alpha_i Z_i}{\sum_{i=1}^N \alpha_i A_i} \rho, \quad (1)$$

where ρ is mass density (g/cm³), A_i and Z_i are atomic mass and atomic number of each element, i , respectively, and α_i is the number of atoms that have atomic number Z_i . For compounds, the atomic number is referred to as effective atomic number, Z_{eff} , which can be classically parameterized as^{52,53}

$$Z_{\text{eff}} = \sqrt[l]{\sum_{i=1}^N r_i Z_i^l}, \quad (2)$$

where r_i is "relative electron fraction" contribution of an element, i ,

$$r_i = \frac{\alpha_i Z_i}{\sum_{j=1}^N \alpha_j Z_j}.$$

In previous work,⁴⁹ the exponent l was studied to optimize the value for the best classification performance for the materials, source spectrum, and system features used. The value of $l = 8.0$

showed the highest classification accuracy, therefore we chose this value for the calculation of reference Z_{eff} values in this work.

2.2 Decomposition of LAC

For a CT system, Alvarez and Macovski¹⁰ presented empirically over the energy region between 30 and 200 keV that the LAC can be decomposed as follows:

$$\mu(E) = a_1 \frac{1}{E^3} + a_2 f_{\text{KN}}(E), \quad (3)$$

where $f_{\text{KN}}(E)$ denotes the Klein–Nishina function defined as

$$f_{\text{KN}}(\varepsilon) = \frac{1 + \varepsilon}{\varepsilon^2} \left(2 \frac{1 + \varepsilon}{1 + 2\varepsilon} - \frac{\ln(1 + 2\varepsilon)}{\varepsilon} \right) + \frac{\ln(1 + 2\varepsilon)}{2\varepsilon} - \frac{1 + 3\varepsilon}{(1 + 2\varepsilon)^2}, \quad (4)$$

and $\varepsilon = E/511$ keV ($\varepsilon = E/m_e c^2$) designates the reduced energy of the incoming photon. The functions $1/E^3$ and $f_{\text{KN}}(E)$ represent the approximation of the energy dependence of the photoelectric absorption and Compton scattering, respectively. With the exception of the absorption edge effect, they further presented that the photoelectric coefficient, a_1 , and the Compton scattering coefficient, a_2 , could be defined as

$$a_1 \approx K_1 \frac{\rho}{A} Z^n, \quad a_2 \approx K_2 \frac{\rho}{A} Z, \quad (5)$$

where K_1 and K_2 are constants, and n is the exponent for the photoelectric cross section in the decomposed LAC (per atom). The n value is optimized for each classification approach that determines how many energy bins are used for the estimation of material features. a_1 and a_2 are expressed with an approximation, and inserting a_1 and a_2 from Eq. (5) in Eq. (3) gives the decomposed LAC as

$$\mu(E) = \frac{Z}{A} \rho (Z^{n-1} p(E) + c(E)), \quad (6)$$

where

$$p(E) = K_1 \frac{1}{E^3}, \quad c(E) = K_2 f_{\text{KN}}(E). \quad (7)$$

$p(E)$ and $c(E)$ denote the photoelectric absorption and Compton scattering basis functions, respectively. Inserting Eq. (1) in Eq. (6), we retrieve a parameterized LAC for a compound as

$$\mu(E) = \rho_e (Z_{\text{eff}}^{n-1} p(E) + c(E)). \quad (8)$$

The basis functions are empirically measured through fitting experimental data. In this work, the basis functions and the exponent n are defined in the calibration step and then used in the calculation of material features, which compose the formulation of the classification method described in Sec. 4.

2.3 Experimental Setup and Materials

The experiments were conducted in the 3D Imaging Center at DTU, Denmark. The X-ray beam was generated by a Hamamatsu source working under the acceleration voltage and the filament current set to 150 kV and 0.5 mA, respectively. The focal spot is 75 μm . An aluminum filter of 2 mm thickness was mounted after the source to suppress photons with energies lower than the detector's energy range. The beam was collimated to a fan beam using a JJ X-Ray IB-C80-AIR slit. Custom built 5-mm-thick tungsten carbide blades placed directly in front of the detector minimize photon scattering and fluorescent radiation. The samples were placed on the rotation stage and scanned between discrete rotations with certain increments over a range of 360 deg.

The value for increments was set depending on the number of projections, for which the classification performance is estimated for each sample. The source to sample distance was set to 500 mm, while the source to detector distance was 701 mm. The radiation integration time of the detector can change between 2 and 100 ms with increments of 10 μ s.

Figure 1 shows the four samples that include groups of materials that were scanned simultaneously, this work also uses samples with individually scanned materials. Figure 1(d) shows the sample containing aluminum, magnesium, and polyetheretherketone (PEEK). This sample is used for the characterization in Sec. 5.3 that tests the classification performance for the raw and corrected data with different integration times from 2 to 100 ms and in Sec. 5.4.

Tables 1 and 2 list the reference and test materials used in the calibration and material feature calculation steps, respectively. The tables include the materials' reference ρ_e and Z_{eff} values that were calculated using Eqs. (1) and (2), respectively. Sample dimensions are described through width \times length for rectangular samples or diameter for circular samples. The plastics are polycarbonate (PC), polymethyl methacrylate (PMMA), polyoxymethylene-C (POM-C), polytetrafluoroethylene (PTFE), polyethylene terephthalate (PET), polyoxymethylene-H (POM-H), and polyvinylidene fluoride (PVDF). The material properties tabulated in the tables will be considered as the reference for the remainder of the paper. The materials vary in the range of $6 \leq Z_{\text{eff}} \leq 15$, which covers the Z_{eff} range of major human organs and tissues,^{56–58} since the most abundant elements in human tissues as well as polymers are H, C, N, and O.⁸ This Z_{eff} range is also relevant for security applications.⁹

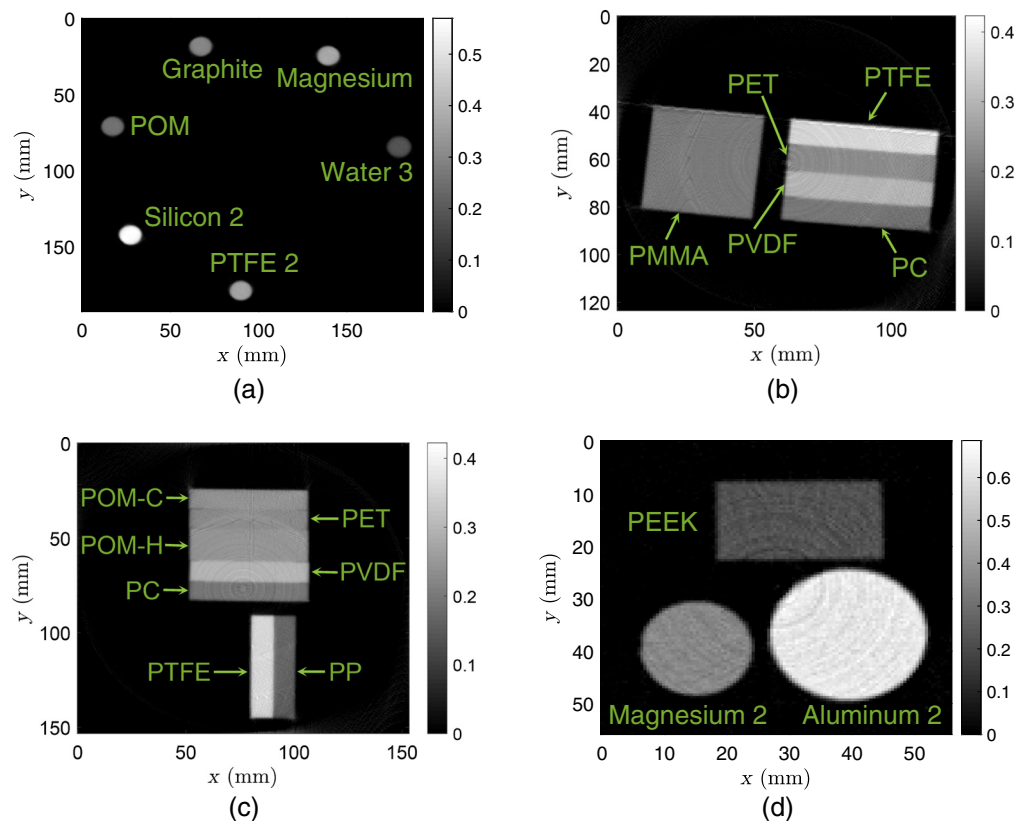


Fig. 1 Reconstruction of samples containing groups of multiple materials. (a)–(c) Samples used in the classifications for which the results are presented in Secs. 5.1–5.3. The sample (a) was borrowed from Busi et al.⁴⁸ The polypropylene (PP) material in the sample (c) is suspected to be mixed with chemical colorants, and therefore to have a higher Z_{eff} than the pure PP. This material was therefore excluded in estimations. (d) Sample being processed in Secs. 5.3 and 5.4. All the 2D reconstructions are performed from 360 projections using the SIRT⁵⁴ (in the illustration, data from the energy bin at 75.1 keV were used). The gray scale bars represent the LACs in unit of cm^{-1} .

Table 1 The reference materials used in the calibration step (see Sec. 4.1), with reference values of ρ_e and Z_{eff} . The ρ mass density values for the plastic materials were measured with uncertainties of $\pm 0.15\%$. The mass densities for the rest of materials represent the theoretical values found in PubChem data.⁵⁵

Material	Chemical formula	Width \times length/ diameter (mm)	ρ (g/cm ³)	ρ_e (e ⁻ mol/cm ³)	Z_{eff}
Graphite	C	12.7	1.8	0.899	6
PC	(CO ₃ C ₁₃ H ₈) _n	8.2 \times 53.5	1.18	0.610	6.82
PMMA	(C ₅ O ₂ H ₈) _n	40 \times 42	1.18	0.636	7.02
POM-C	(CH ₂ O) _n	9 \times 53.5	1.41	0.753	7.40
PTFE	(C ₂ F ₄) _n	9 \times 53.3	2.16	1.035	8.70
N,N-Dimethylhydrazine	C ₂ H ₈ N ₂	67	0.791	0.447	6.44
Ethylenediamine	C ₂ H ₈ N ₂	67	0.90	0.509	6.44
Acetone 2	C ₃ H ₆ O	54	0.785	0.432	6.90
Nitrobenzene	C ₆ H ₅ NO ₂	49	1.20	0.624	7.00
Ethanol 96%	C ₂ H ₆ O (96%)	67 \times 67	0.798	0.450	7.06
Methanol	CH ₃ OH	20	0.792	0.446	7.29
Hydrazine solution	H ₄ N ₂ (35%)	54	1.0	0.561	7.43
Nitromethane	CH ₃ NO ₂	20	1.14	0.597	7.50
Water	H ₂ O	20	0.997	0.554	7.78
Water 3	H ₂ O	12.7	0.997	0.554	7.78
Hyd. peroxide 2	H ₂ O ₂ (50%)	73 \times 74	1.22	0.661	7.83
Magnesium 2	Mg	18	1.74	0.859	12
Aluminum 2	Al	25	2.70	1.3	13
Aluminum 3	Al	20 \times 20	2.70	1.3	13
Silicon	Si	25	2.33	1.161	14

2.4 Detector and Data Correction for Spectral Distortion

The detector adopted for the experiments is MultiX ME-100 v2 manufactured by Detection Technology S.A.S. in Moirans, France. We use a system of five detector modules, each module has a 1×128 linear array of pixels sized 0.8×0.8 mm². The detector has 128 spectral energy bins, each with a width of 1.1 keV, which are evenly distributed between 20 and 160 keV. The energy resolution of the detector operating at high x-ray fluxes is 6.5% (8 keV at 122 keV).²³ The detector has a CdTe sensor with 3 mm thickness. Incident photons strike a collective cathode being composed of a continuous metal film. The sensor has pixelated anodes with significantly smaller size, which are located on readout electronics.

The spectral response of photon counting detectors is severely distorted by a range of physical effects occurring inside the CdTe sensor crystal. These energy- and flux-dependent effects decrease the energy resolution of PCDs and induce distortion in measured LAC curves. An x-ray photon absorbed near a pixel border generates an electron charge cloud which may split between neighboring detector pixels. As a result, the high-energy x-ray photon is falsely counted as two photons with lower energies, and this physical phenomenon is called charge sharing. Another phenomenon is related to x-ray fluorescence. Detector sensor materials Cd and Te present

Table 2 The test materials used in the material feature calculation step (see Sec. 4.2), with reference values of ρ_e and Z_{eff} . The ρ mass density values for the plastic materials were measured with uncertainties of $\pm 0.15\%$. The mass densities for the rest of materials represent the theoretical values found in PubChem data.⁵⁵

Material	Chemical formula	Width \times length/ diameter (mm)	ρ (g/cm ³)	ρ_e (e ⁻ mol/cm ³)	Z_{eff}
PET	(C ₁₀ H ₈ O ₄) _n	9 \times 53.5	1.39	0.721	7.09
POM-H	(CH ₂ O) _n	15.5 \times 53.3	1.43	0.763	7.40
PVDF	(C ₂ H ₂ F ₂) _n	9 \times 53.5	1.79	0.896	8.40
PTFE 2	(C ₂ F ₄) _n	12.7	2.2	1.056	8.70
2-Butanone	C ₄ H ₈ O	83	0.805	0.447	6.76
Acetone	C ₃ H ₆ O	20	0.785	0.432	6.90
Methanol 2	CH ₃ OH	81	0.792	0.446	7.29
Ethanol 40%	C ₂ H ₆ O (40%)	67 \times 67	0.947	0.532	7.63
Water 2	H ₂ O	51 \times 51	0.997	0.554	7.78
Nitric acid	HNO ₃ (65%)	83	1.39	0.714	7.80
Hyd. peroxide	H ₂ O ₂ (50%)	20	1.22	0.661	7.83
Magnesium	Mg	12.7	1.74	0.859	12
Aluminum	Al	25	2.70	1.3	13
Silicon powder	Si	48	0.65	0.324	14
Silicon 2	Si	12.7	2.33	1.161	14

K-edges at 26.7 and 31.8 keV, respectively. Incoming x-rays at an energy E can expel K-electrons of the CdTe sensor crystal when the photon energy is larger compared to the K-shell binding energies. The vacant K-shells are instantly reoccupied, and the fluorescence K-shell photons with energy E_{fl} are emitted and re-absorbed in some cases. The fluorescence photons are registered in the primary detector pixel or in adjacent pixels (K-escape). As a result, the incoming photons are registered at an energy $E - E_{\text{fl}}$, and the consequent peak in the energy spectrum is called K-escape peak. Thus, high-energy x-rays are again recorded at lower energies, leading to a decrease in energy separation and also spatial resolution.

Charge sharing and K-escape are border interactions. The contribution of these phenomena to the overall detector response decreases as the detector pixel size increases, and this can improve energy discrimination. However, the number of incident photons that strike the same pixel increases in time if the pixel has larger size. This may result in the overlapping of pulses created by two photons that are recorded as one photon at a very high energy. This effect is called pulse pile-up. Pulse pile-up can cause nonlinear detector counting statistics and eventually detector saturation.⁵⁹ The contribution of this effect to the total detector response can be reduced with designing smaller pixels; however, this may result in increased charge sharing and K-escape. Discovering the best size of the detector pixels to steady charge sharing, K-escape, and pulse pile-up is very important in making a PCD.

Charge carriers that are counted by one detector pixel may again produce a pulse in the adjacent pixel. This phenomenon is called WP cross talk and gives rise to the source spectrum at energies lower than 30 keV.⁵⁰ The effects such as electronic noise⁶⁰ and Compton scattering of the incoming photons in the detector crystal are another problems of PCDs. Both effects have less contributions to the detector signal compared to the other effects.

CdTe detectors are also subjected to another challenge that is charge trapping. Some of charge carriers are trapped in crystal lattice defects or impurities, which are nonuniformly distributed.⁶¹ This results in the effect called ICC. The ICC becomes visible in the spectrum at energies higher than 60 keV.⁶² The electrons and holes move at drift velocities $v_e = \mu_e E_e$ and $v_h = \mu_h E_e$ toward the collective cathode and pixelated anodes, respectively. μ_e and μ_h are the electron and hole drift mobilities, respectively, and E_e is the external electric field. The holes drift with significantly smaller mobility than electrons. The electrons have 1000 cm²/V of the drift mobility, whereas the holes have 80 cm²/V.⁶³ This leads to more severe trapping of the slow holes than the electrons. The influence of hole trapping is typically reduced by designing a CdTe detector with much smaller pixelated anodes than the crystal thickness. This gives comparatively far less contribution of the hole transport to the total signal and thus reduces the ICC effect.⁶⁴ Moreover, the trapped holes create the accumulation of positive charges in the crystal, which can change the external electric field distribution over time and distort the characteristics of the charge collection. This effect is called polarization and also can lead to ICC.^{61,65} Polarization might cause noticeable ring artifacts in the reconstruction images at higher photon fluxes,⁵⁹ and a rapid decrease in signal pulses above a definite high flux rate.⁶⁶

In the correction algorithm, using the simulated detector response matrix the distorted spectrum is first corrected for the flux-independent effects, such as charge sharing, WP cross talk, x-ray fluorescence (escape peaks), Compton scattering, and electronic noise. Flux-independent effects are corrected using an inverse detector response matrix \mathbf{M}_C of size $N \times N$, where N is the number of energy bins. The raw data are represented as a matrix \mathbf{I}_R of dimension $N \times J$, where J is the number of detector pixels. The matrix for corrected data for each pixel is obtained as⁵⁰

$$\mathbf{I}_C = \mathbf{M}_C \mathbf{I}_R. \quad (9)$$

The inverse detector response matrix is decomposed into the individual detector response matrices and can be expressed as⁵⁰

$$\mathbf{M}_C = (\mathbf{D}_C \mathbf{D}_E \mathbf{D}_{WP})^{-1}, \quad (10)$$

where \mathbf{D}_{WP} , \mathbf{D}_E , and \mathbf{D}_C are the detector response matrices corresponding to WP cross talk, Compton scattering and electronic noise, and charge sharing effects, respectively. The WP cross talk is first calculated to correct distortion at low energies, while the charge sharing is lastly corrected.

For each pixel's response to x-ray illumination, a Monte Carlo simulation is employed to calculate the total detector response matrix, which is dependent on the incident x-ray energy and location of the photon's energy deposition. The location of photon absorption is considered as a function of depth in the sensor under the probability distribution function defined by the reference LACs, which are obtained from the National Institute of Standards and Technology (NIST) cross-sections.⁶⁷ In the simulation, the escape peaks phenomenon occurring due to x-ray fluorescence is first defined, by assuming that the emitted fluorescence photons are randomly directed and absorbed at a certain travel distance. \mathbf{D}_{WP} , \mathbf{D}_E , and \mathbf{D}_C detector response matrices are then computed separately based on 2D histograms of the registered and actual incident photon energy in the simulation. In the calculation model of the charge sharing factor, the excited electron cloud is split between two adjacent pixels based on a 1D Gaussian distribution that is aligned with the detector array. The excited charge cloud can induce current in the adjacent pixels, and the amount of WP cross talk is proportional to the amount of current. A simplified model presented in Ref. 68 is used for calculating WP cross talk, in which the detector is considered as the detector surfaces being composed of two infinite parallel sheets. The model employs the approach of reflected dipole layers (mirror charges), which assumes that WP cross talk is defined as an infinite sum of the WP elementary functions corresponding to the reflected dipole layers distributed at equal distances dependent on the crystal depth.

Matrix inversion requires that the matrix is invertible, but a robust correction furthermore requires that the detector response matrix is well conditioned. Since the three detector response matrices are calculated in advance, the condition number can be found before the correction is utilized. For the case reported here, the condition number for the three matrices is between 1 and

2, which means that the detector response matrices are well conditioned and the subsequent matrix multiplication is not overly sensitive to noise. An alternative but time consuming method for an ill-conditioned detector response matrix is an iterative approach that estimates the corrected signal by successively applying the noninverted detector response matrices to a guessed response until the resulting spectra matches the acquired spectra.

Flux-dependent models such as the pulse pileup and ICC are then considered for correction. The model presented by Plagnard⁶⁹ is employed to correct for the pile-up phenomenon. Note that this model is independent of pulse type whether it is unipolar or bipolar. The pile-up effect of photon with energy E_n on the rest of energies E_x of the measured spectrum $I_R(E)$ gives the respective pile-up spectrum $I_P(E_{nx})$, which is defined for the whole range of x as^{50,69}

$$E_{nx} = E_n + E_x, \tag{11}$$

$$I_P(E_{nx}) = \frac{I_R(E_n)}{I_R(E)_{\max}} C_P I_R(E_x), \tag{12}$$

where C_P is a coefficient for defining pile-up probability. It is assumed that two photons with energies E_n and E_x in the measured spectrum are recorded as one photon with energy E_{nx} in the pile-up spectrum. Dreier et al.⁵⁰ use an automatic fitting method to compute this coefficient using the spectral LACs of aluminum. The pile-up spectrum is deducted from the measured spectrum, and the result is added to $\sum_x I_P(E_{nx})$ summed over the whole range of x . This gives the corrected spectrum $I_C(E_n)$ of the energy bin n ⁵⁰

$$I_C(E) = I_R(E) - I_P(E), \tag{13}$$

$$I_C(E_n) = I_C(E_n) + \sum_x I_P(E_{nx}). \tag{14}$$

To obtain the whole corrected spectrum, the same modeling is applied for each increment of n changing from the initial to final values. The correction algorithm has been applied successfully to this detector for fluxes up to 5 Mph/s/mm². The MultiX’s readout electronics are constructed to work well at fluxes higher than 1 Mph/s/mm².^{23,60} We refer the reader to Dreier et al.⁵⁰ for more details of the correction algorithm.

The materials studied in this work are relevant to the security domain, but they also resemble the atomic number and densities of organic tissues. The ability to contrast the used materials is thus directly applicable in medical imaging. The contrast materials used in medical imaging, such as calcium, iodine, gadolinium, or tantalum, have not been investigated. These materials with higher atomic numbers ($Z_{\text{eff}} \geq 20$) may exhibit absorption edges above the low-energy threshold described in Sec. 3.2. However, the correction algorithm is shown to work for these materials in the same way as described in this study. Tantalum, for example, was studied in Ref. 50, and the distorted attenuation curve was accurately corrected in the energy range used in this work.

2.5 Sinogram Generation

The correction of the raw data is followed by converting the photon counts I_k of energy bin k to line integrals L_k , i.e., sinograms, based on Lambert–Beer’s law as follows:

$$L_k(\vec{x}) = -\log \frac{I_k(\vec{x})}{I_{0,k}(\vec{x})}, \quad k = 1, 2, 3, \dots, K; \tag{15}$$

where $I_{0,k}$ is the flat-field photon counts for energy bin k , i.e., the projection without the sample being placed, K is the number of energy bins used, and \vec{x} denotes the 1D detector pixel array.

3 Image Reconstruction Algorithm and LAC Extraction

In this section, we briefly describe the joint reconstruction algorithm used to reconstruct the samples from experimental data. We also present the LAC extraction and energy bins rebinning between low and high energy thresholds. Lastly, a tool for analyzing the reconstruction image quality estimated from the raw and corrected data is introduced.

3.1 Joint Reconstruction

Suppose spectral CT measurements consist of a stack of K energy-resolved sinograms denoted by $\mathbf{p}_1, \dots, \mathbf{p}_K \in \mathbb{R}^G$, with K being the number of energy bins and G being the number of detector pixels multiplied by the number of projection angles. We target to reconstruct K attenuation images from the spectral sinograms, $\mu_1, \dots, \mu_K \in \mathbb{R}^J$, with J being the number of image pixels for each energy bin E_k ($k = 1, 2, \dots, K$). Energy-resolved LACs are retrieved directly from the spectral reconstructions. We denote a stack of the spectral sinograms by a vector $\mathbf{p} \in \mathbb{R}^{KG}$, and a stack of K reconstructions by $\mu \in \mathbb{R}^{KJ}$. The LAC for the energy bin E_k and the j 'th image pixel ($j = 1, 2, \dots, J$) is represented by $\mu_{k,j}$.

An operator, known as the forward-projection, maps the images onto the sinogram domain, and the forward-projection is commonly formulated as a linear operator \mathbf{A} such that $\mathbf{A}\mu = \mathbf{p}$. Here, we use the same forward-projection operator for each energy bin and \mathbf{A} is the stack of such operators. This formulation enables comparing the estimation with the sinogram data \mathbf{p} and we want to minimize the reprojection error (distinction between the synthesized and observed sinogram) in L_2 norm as follows:

$$\mathcal{G}(\mathbf{A}\mu) = \frac{1}{2} \|\mathbf{A}\mu - \mathbf{p}\|_2^2. \tag{16}$$

To deal with noisy data and a small number of projection angles and obtain better reconstruction by taking advantage of multispectral dimensionality of reconstructions, we consider a regularization term by imposing *a priori* knowledge on the solutions. We employ a vectorial total variation scheme called L_∞ -VTV that correlates the image gradients using maximum norm over multienergy bins as follows:

$$\mathcal{R}_{\text{VTV}}^{L_\infty}(\mu) := \sum_{j=1}^J (\max_{1 \leq k \leq K} |\nabla_x \mu_{k,j}| + \max_{1 \leq k \leq K} |\nabla_y \mu_{k,j}|), \tag{17}$$

where $\mu_{k,j}$ represents the LAC value for the k 'th energy bin and j 'th image pixel, and ∇_x and ∇_y denote the gradient operators with respect to x and y axes, respectively. We aim to minimize the sum of the data fitting term [Eq. (16)] and the regularization term [Eq. (17)] with a weighting parameter λ between two terms as follows:

$$\min_{\mu \geq 0} \lambda \mathcal{G}(\mathbf{A}\mu) + \mathcal{R}_{\text{VTV}}^{L_\infty}(\mu), \tag{18}$$

where a non-negativity constraint is imposed on μ such that the LAC values should be non-negative.

A positive weighting parameter defines the strength of the L_∞ -VTV regularization term and thus controls the trade-off between a good match to spectral sinogram data and a smooth reconstruction in both the spatial and spectral dimensions. The L_∞ -VTV norm correlates the gradients strongly over spectral dimension, rejecting outliers in gradient magnitudes. The reconstruction algorithm uses additional information across the spectral dimension and thus can enhance the reconstruction quality. The noise in one energy bin resulting in blur in a definite edge can be suppressed by the information in the other bins of the same edge. We refer the reader to Jumanazarov et al.⁷⁰ for more details on the reconstruction algorithm.

The image reconstruction algorithm is applicable to any type of materials including heterogeneous materials. After the reconstruction step, we manually segment the reconstructed image, and it requires more effort to segment heterogeneous materials, compared to homogeneous

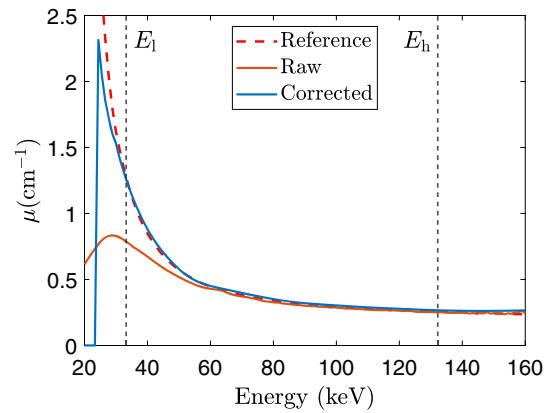


Fig. 2 Spectral LACs for magnesium obtained from the raw and corrected data. The reference LACs were obtained from NIST cross-sections.⁶⁷ The vertical black dash-dotted lines represent the low and high energy thresholds, E_l and E_h , remaining the same for all materials being estimated.

materials. However, with the correct segmentation we expect that the classification accuracy will not be significantly affected.

3.2 LAC Extraction

After the energy-resolved reconstruction and manual segmentation, the LAC value of a segment is calculated from the attenuation value histogram based on normal distribution fitting method within a region of interest of a sample.⁴⁹ The LAC extraction is performed for each material and energy bin. Figure 2 presents an example of magnesium's spectral LAC computed from both the raw and corrected data with the correction algorithm, and two spectral LAC curves are compared to the reference curve. The correction algorithm largely restores the LAC toward the reference curve at the low energies, however, fails to correct for additional spectral distortions at lower and higher energies. One reason for this could be because of detector flux variation and photon starvation, i.e., complete attenuation of photons.⁵⁰ The energy bins in which the LAC is deviating from the reference values even after applying the correction algorithm are excluded in the later processing by inserting the low- (E_l) and high-energy (E_h) thresholds. The thresholds are set to $E_l = 33.2$ keV and $E_h = 132.2$ keV and kept constant for all the samples scanned and processed. The low energy bins have significantly lower photon counts due to a higher absorption from the source filter. Since the LACs are computed according to Eq. (15), a step in the correction algorithm overcomes the influence of the resulting NaNs, Infs, and very low counts, by setting the LAC to 0 for the low energy bins. Therefore, the corrected LAC curve in Fig. 2 has a sharp drop-off around 25 keV.

3.3 Rebinning Energy Bins

In this work, we test the classification performance with two approaches, in which the data are rebinned from 90 energy bins into 2 and 15 bins. The rebinning is performed by integrating the photon counts between a low- and a high-energy thresholds. The aim of rebinning is first to increase photons statistics of each bin, and second to decrease the data amount, and thereby the computation time for image reconstruction. The 15 energy bins are distributed with equal bin width between 33.2 and 132.2 keV. In previous work,⁴⁹ we estimated the classification performance with 2, 15, 30, 45, and 90 energy bins. We found that 30, 45, and 90 energy bins did not lead to better improvement in the classification performance compared to 15 energy bins. We concluded that a higher number of bins decrease the energy bin width below the detector's energy resolution (8 keV) but lead to lower photon statistics, and thereby decrease signal-to-noise ratios in each bin. Therefore, we employ 15 energy bins in this work, with energy bin widths (6.6 keV) slightly below the detector's energy resolution. The approach of 15 energy

bins shows spectral LAC curves that can be seen in Fig. 2, while the two bins approach only give two data points in the attenuation spectrum.

The approach of two energy bins consists of nonoverlapping low and high energies, which are separated by a gap corresponding to the interval between 63.0 and 79.5 keV. We chose this gap width to have it larger than the detector's energy resolution, and the gap position such that it is in the middle of the used energy range. To separate it from a simple rebinning into two bins, we refer to it as a bienergy approach in the remainder of the article. In the bienergy approach, photons with energies within this gap are discarded, but still the classification performance is found to improve.^{49,71,72} The other advantages of the bienergy approach are less sensitivity to detector artifacts and more robustness to high noise levels. Furthermore, reconstructing only two energy bins makes this approach more computationally efficient. Spectral CT thus has a trade-off between spectral channelization and noise levels. In addition to rebinning, we also use the joint reconstruction algorithm to reduce reconstruction artifacts due to increased noise levels. The method L_∞ -VTV employs additional information across the spectral dimension as described in Sec. 3.1.

3.4 Correlation Coefficient for Evaluation of Reconstruction Quality

We measure the reconstruction quality with a correlation coefficient r that determines how the reconstructed image μ is linearly related to the ground-truth image \mathbf{v} and is defined for the energy bin k as

$$r_k = \frac{\sum_j (\mu_j - \bar{\mu})(v_j - \bar{v})}{\sqrt{\sum_j (\mu_j - \bar{\mu})^2 \sum_j (v_j - \bar{v})^2}}, \quad (19)$$

where $\bar{\mu}$ and \bar{v} are the mean LACs computed from the LACs for each image pixel, and μ_j and v_j represent the j 'th image pixel values for μ and \mathbf{v} , respectively. To calculate the correlation coefficient, the ground-truth images are created with the mean LAC for each material and energy bin. The mean LAC is computed from the attenuation histogram based on the normal distribution after the sample is reconstructed using 360 projections and the simultaneous iterative reconstruction technique (SIRT).⁵⁴

3.5 L-Curve

We also investigate the L-curve criteria^{73,74} on both raw and corrected data. The L-curve criteria is a plot of the two-norm of maximum gradients, $\|\mu_\lambda\|_{L_\infty\text{-VTV}}$ [Eq. (17)], as a function of the two-norm of the corresponding residual vector, $\|\mathbf{A}\mu_\lambda - \mathbf{p}\|_2$ [Eq. (16)], both dependent on the weighting parameter λ . Based on the L-curve, one can find the optimal λ for a regularized reconstruction without the ground truth image of a sample. The plot is expected ideally to appear L-shaped, and the λ value corresponding to the point exactly at the knee of the curve represents the optimal λ . The values on the flat and vertical lines result in over-regularized and under-regularized solutions, respectively. Therefore, we test this tool for the raw and corrected data to explore how the optimal λ found from the L-curve matches with those from the correlation coefficient tool. We use a linear-linear scale for plotting the L-curve.⁷⁴

4 Method to Material Classification

In this section, for the ease of the reader we briefly give a description of the classification method, the SIMCAD, that we previously presented in detail in Ref. 49. This method estimates ρ_e and Z_{eff} parameters of materials from spectral CT measurements.

4.1 Calibration of Parameters in LAC

Based on Eq. (8), LAC of a material m for each energy bin E_k can be represented as

$$\mu_m(E_k) = \rho_{e,m}(Z_{\text{eff},m}^{n-1}P(E_k) + c(E_k)), \quad (20)$$

where $m = 1, 2, \dots, M$, $k = 1, 2, \dots, K$ with M and K being the number of reference materials and energy bins, respectively. $p(E_k)$ and $c(E_k)$ denote photoelectric absorption and Compton scattering basis functions, respectively. The basis functions found through the calibration step are energy-dependent and remain the same for all samples being scanned.

We also optimize the parameter n together with the basis functions for better estimation of the material features. To solve Eq. (20), positivity constraints are imposed for all basis functions and n on the solution, and the nonlinear objective function is constructed as

$$\min_{0 \leq p_1, c_1, \dots, p_K, c_K, n} \sum_{m=1}^M \sum_{k=1}^K (\mu_m(E_k) - \rho_{e,m} (Z_{\text{eff},m}^{n-1} p_k + c_k))^2, \quad (21)$$

where $p_k = p(E_k)$ and $c_k = c(E_k)$. Equation (21) is optimized using a nonlinear least square solver through the trust region method.⁷⁵ Initial constraints were selected as $p_k^0 = 0.5$, $c_k^0 = 0.5$, and $n^0 = 3.6$ for all energy bins, k . No particular dependency on the initial constraints was observed. Note that the calibration step is independently performed for the raw and corrected data. The formulation of the classification method is compatible with an arbitrary number of energy bins. We use the reference materials listed in Table 1 to compute the calibration parameters (p_k , c_k , and n) from Eq. (21). The (ρ_e , Z_{eff}) values are then calculated based on these calibration parameters.

4.2 Calculation of Material Properties

We estimate the ρ_e and Z_{eff} parameters of the test materials using the calibration parameters, $p(E_k)$, $c(E_k)$, and n , and the extracted LACs of the test materials $\mu(E_k)$. For M and K being the total number of the test materials and energy bins, respectively, Eq. (20) can be reformulated as a linear system of equations as

$$\begin{pmatrix} \vec{p} & \vec{c} & & & \\ & & \ddots & & \\ & & & \vec{p} & \vec{c} \end{pmatrix} \begin{pmatrix} z_1 \\ \rho_{e,1} \\ \vdots \\ z_M \\ \rho_{e,M} \end{pmatrix} = \begin{pmatrix} \vec{\mu}_1 \\ \vdots \\ \vec{\mu}_M \end{pmatrix}, \quad (22)$$

where z_m represents a temporary variable added instead of $\rho_{e,m} Z_{\text{eff},m}^{n-1}$, and $\vec{p} = (p_1, \dots, p_K)^T$, $\vec{c} = (c_1, \dots, c_K)^T$ and $\vec{\mu}_m = (\mu_m(E_1), \dots, \mu_m(E_K))^T$. The size of the linear matrix in the above equation is $(M \times K)$ -by- $(2 \times M)$ and the number of unknowns equals $2 \times M$. Imposing the positivity constraint on the solution, we retrieve the vector $(z_1, \rho_{e,1}, \dots, z_M, \rho_{e,M})$ that minimizes the norm in the linear least square problem. Z_{eff} values of all the test materials are then obtained by

$$Z_{\text{eff},m} = \left(\frac{z_m}{\rho_{e,m}} \right)^{\frac{1}{n-1}}. \quad (23)$$

The classification accuracy is computed based on the percent relative deviation defined as

$$\Delta Z_{\text{eff}}^{\text{rel}} = 100\% \cdot \frac{Z_{\text{eff}}^{\text{est}} - Z_{\text{eff}}^{\text{ref}}}{Z_{\text{eff}}^{\text{ref}}}, \quad (24)$$

$$\Delta \rho_e^{\text{rel}} = 100\% \cdot \frac{\rho_e^{\text{est}} - \rho_e^{\text{ref}}}{\rho_e^{\text{ref}}}, \quad (25)$$

where superscripts est and ref represent the estimated and reference values, respectively. To solve Eq. (22), we employ the test materials listed in Table 2, for which the classification results are presented in Secs. 5.1 and 5.2.

5 Results and Discussions

Note that the classification results presented in Secs. 5.1 and 5.2 were obtained with the total integration time per projection set to 8 s. This yields an effective frame rate of 80 frames per projection, as the integration time for each frame is 100 ms. The value of integration time is mentioned in the other subsections in the results section. The materials within the samples presented in Figs. 1(a)–1(c) were scanned in groups, while the other materials listed in Tables 1 and 2 were scanned separately.

5.1 Classification Performance with Respect to the Number of Energy Bins

Figures 3(a) and 3(b) present the relative deviations for the raw and corrected data, obtained with the bi- and 15 energy bins approaches. The shown results for ρ_e and Z_{eff} computed as a function of weighting parameter λ were obtained from 12 projections. With the 15 energy bins approach, the corrected data give the mean relative deviations of 3.4% for ρ_e and 2.7% for Z_{eff} (at $\lambda = 16$), whereas the raw data result in the deviations of 5.6% and 10.3% (at $\lambda = 4$), respectively. Note that the mean relative deviations correspond to the optimal λ values that provide the maximal classification performance for both approaches. With the bienergy bins approach, the corrected data give the mean relative deviations of 2.6% for ρ_e and 3.9% for Z_{eff} (at $\lambda = 6$), while the raw data yield 8.0% and 12.4% (at $\lambda = 2$), respectively. Thus, the raw data give significantly lower classification accuracy than the corrected data in both approaches. With the corrected data, the 15 energy bins appear to give better classification performance compared with the bienergy bins. We assume that the classification accuracy could be improved by optimizing the position of the energy separation gap in the bienergy bins approach. Since it is time-consuming to compute the reconstructions for a wide range of the materials, gap positions, and weighting parameters, and the aim of this paper is to present the difference in the classification accuracy between the raw and corrected data, we only used a single gap position as introduced in Sec. 3.3.

Figure 3(c) shows the classification results obtained with the two noise cases after Gaussian noise with $\sigma = 0.15$ was added to all the samples and to all the energy bins. In case 1, the noise is added to the raw data and the resulting noisy data is not corrected, and in case 2 the noise is added to the raw data and the resulting noisy data is corrected. Case 1 gives the mean relative deviations of 6.5% for ρ_e and 11.1% for Z_{eff} (at $\lambda = 2.0$), while case 2 yields those of 3.8% and 4.0% (at $\lambda = 20.0$), respectively.

The classification accuracy thus relies on how the measured LAC fits our parameterized LAC defined in Eq. (20). In previous work, using the bin-by-bin SIRT reconstruction algorithm we found that the bienergy bins approach significantly deteriorates classification performance for the raw data.⁴⁹ Figure 4 presents (ρ_e, Z_{eff}) charts of reference and estimated values for the test materials tabulated in Table 2, obtained with raw and corrected data. The results correspond to the optimal λ values giving the maximal classification performance with the 15 energy bins

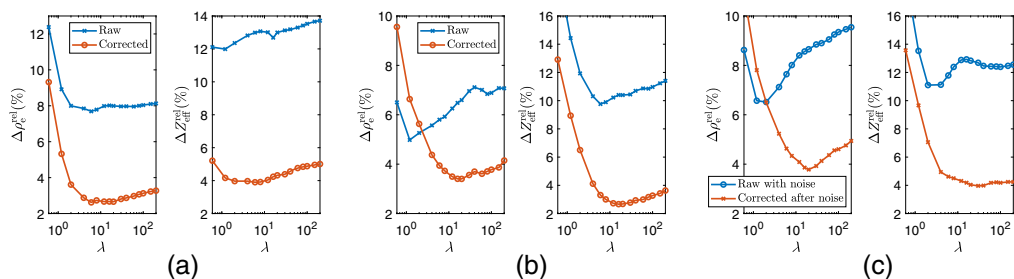


Fig. 3 The relative deviations as a function of weighting parameter λ for ρ_e and Z_{eff} , obtained with the (a) bienergy bins, (b) 15 energy bins, and (c) 15 energy bins for the two noise cases. In the frame (c), Gaussian noise with $\sigma = 0.15$ was added to all the energy bins; in case 1 the noise is added to the raw data and the resulting noisy data is not corrected, and in case 2 the noise is added to the raw data and the resulting noisy data are corrected. The image reconstructions were performed from 12 projections. The graphs show the mean absolute values of relative deviations for each material listed in Table 2. Note the logarithmic scale in the x-axis.

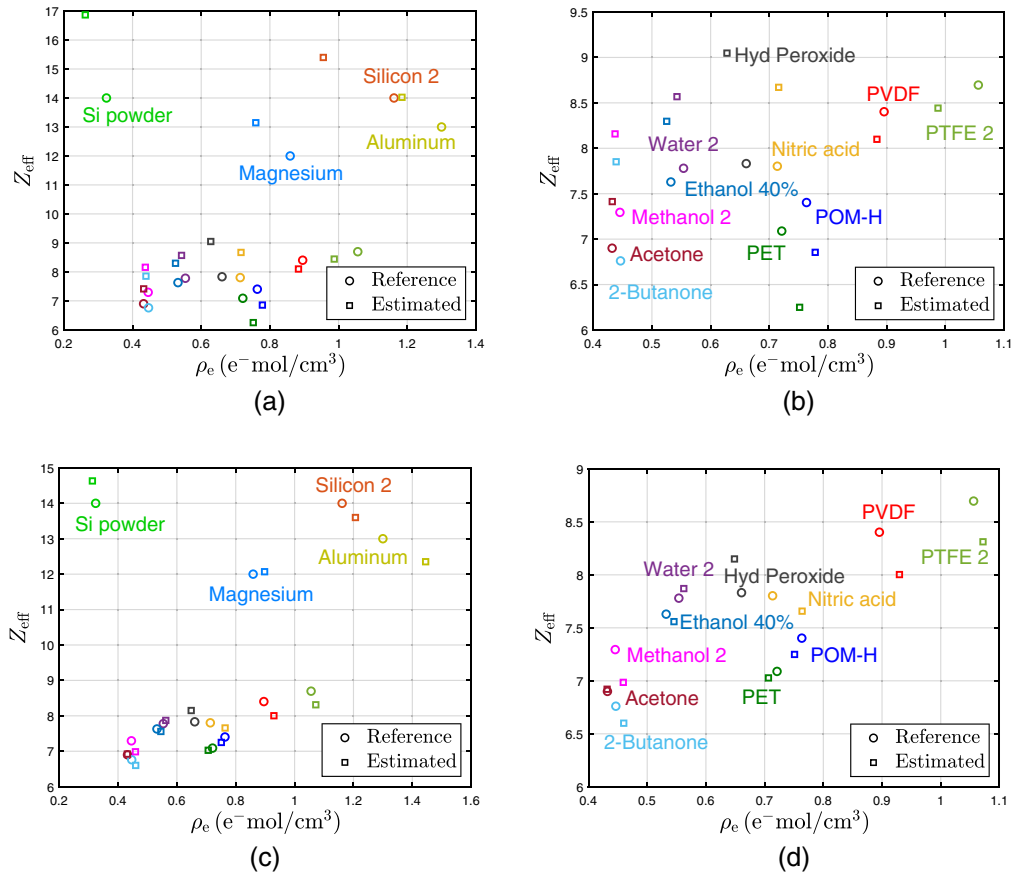


Fig. 4 Estimates from measurements and reference (ρ_e , Z_{eff}) charts obtained with the 15 energy bins approach. (a) The results obtained with the raw data; and (b) an enlarged version of the lower part of the frame (a) is shown to avoid overlap of the material labels. (c) The results obtained with the corrected data; and (d) an enlarged version of the lower part of the frame (c) is shown. The energy-resolved reconstructions were performed from 12 projections and $\lambda = 16$.

approach shown in Fig. 3(b). For the corrected data, the absolute values of relative deviations in ρ_e estimation are lower than 4.5% for all the materials, except for nitric acid and aluminum which have the deviations of -7.0% and -11.2% , respectively. The deviations for Z_{eff} are below 5.0% for all the materials. We found that excluding flux-dependent widening of the detector’s resolution in the correction algorithm improves the correction at low LACs, and thereby significantly reduces the large error in the estimation of aluminum’s ρ_e . We expect that more accurate empirical measurement of constants in the resolution widening correction part based on laboratory data would also improve the accuracy for the high density aluminum. The chart shows that for some materials the relative deviations for the raw data are significantly larger than for the corrected data.

Samples in medical imaging are usually mixtures composed mostly of body tissues with a much lower concentration of a highly attenuating medium. One example is iodine-based contrast agents. The intravascular administration of such agents helps improve image contrast of an explored body region, where the initial atomic number and density of different tissues or organs are very similar but have a different amount of affinity to the contrast agent. A higher contrast helps to differentiate and detect abnormalities from contrast enhanced CT images. The spectral LACs calculated from NIST cross-sections⁶⁷ show that pure water and water-iodine mixtures with iodine concentrations of 5 to 20 mg/cm³ can be discriminated within the detector’s energy range and yield the highest contrast at low energies. Therefore, we can expect that such mixtures can also be discriminated based on Z_{eff} from spectral CT measurements. Support for this expectation can also be found in the literature.^{76,77}

5.2 Classification Performance with Respect to the Number of Projections

The classification performance with raw and corrected data has been evaluated for different numbers of projections. Using a lower number of projections for image reconstruction will enable more rapid scanning and lower radiation exposure time. Figure 5 presents the mean relative deviations for ρ_e and Z_{eff} as a function of weighting parameters λ , obtained with 360, 36, and 7 projections. The results from the raw and corrected data were computed using 15 energy bins. Table 3 shows the classification results corresponding to the optimal λ values. For all numbers of projections, the spectral data correction appears to significantly enhance the estimation accuracy.

Figure 6 illustrates the image reconstructions performed with 360, 36, 12, and 7 projections, obtained from the corrected data. As expected, the reconstruction quality deteriorates as the number of projections decreases. Note that the materials in the reconstruction samples were

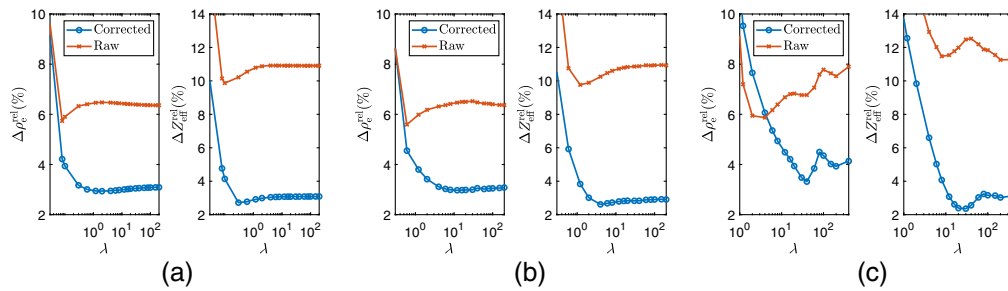


Fig. 5 The relative deviations as a function of weighting parameter λ for ρ_e and Z_{eff} , obtained with (a) 360, (b) 36, and (c) 7 projections. The graphs show the mean absolute values of relative deviations for each material listed in Table 2. Note the logarithmic scale in the x-axis.

Table 3 The estimation of the material properties from raw and corrected data for different numbers of projections, reconstructed at the indicated optimal λ value. See Figs. 3 and 5 for the classification results from the whole range of λ .

Number of projections	Raw			Corrected		
	λ	$\Delta\rho_e^{\text{rel}}$ (%)	$\Delta Z_{\text{eff}}^{\text{rel}}$ (%)	λ	$\Delta\rho_e^{\text{rel}}$ (%)	$\Delta Z_{\text{eff}}^{\text{rel}}$ (%)
360	0.1	5.9	9.9	0.6	3.0	2.8
36	1.2	6.0	9.8	6	3.0	2.7
12	4	5.6	10.3	16	3.4	2.7
7	8	6.4	11.5	30	3.5	2.4

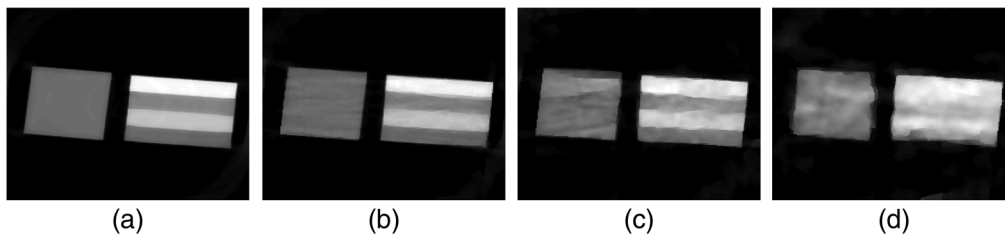


Fig. 6 L_{∞} -VTV reconstructions from (a) 360 ($\lambda = 0.6$), (b) 36 ($\lambda = 6$), (c) 12 ($\lambda = 8$), and (d) 7 projections ($\lambda = 16$) (in the illustration, data from the energy bin at 48.7 keV were used). The weighting parameter mentioned above is used for each reconstruction shown. The reconstruction sample is described in Fig. 1(b).

manually segmented based on the reconstruction from 360 projections to extract LACs. In the seven-projection case, the image edges of different materials are not preserved, and therefore not easy to segment. The reconstruction edges of different materials in the 12-projection case are sharper and allow material segmentation. The reconstructions from 360 and 36 projections show edges that are more accurate and well-preserved than those from 12 projections. However, the classification results of 12 projections are comparable to those of 360 and 36 projections. The weighting parameter λ used for the reconstructions shown in Fig. 6 were chosen based on image quality perceived by human eyes for illustration and may differ noticeably between different experimental samples. It is still an unsolved question how to automatically set the optimal λ for reconstruction and classification. It is expected that L_∞ -VTV reconstruction algorithm works for any type of CT data including clinical data with 12 projections.

5.3 Classification with Different Integration Times

To test performance of the spectral correction for data with different radiation dose levels, the sample illustrated in Fig. 1(d) was scanned with different integration times of the detector and thus different dose levels. Figure 7 shows the correlation coefficients and L-curves with respect to λ , obtained with the raw and corrected data for 10 and 2 ms. The results in this section were obtained using 12 projections and 15 energy bins. Even though the raw data leads to significant deviations in the LACs as shown in Fig. 2, the raw and corrected data present similar correlation coefficients, i.e., similar reconstruction quality. The case of 10 ms shows that both the raw and corrected data have good agreement between the λ value found from the corner of the L-curve

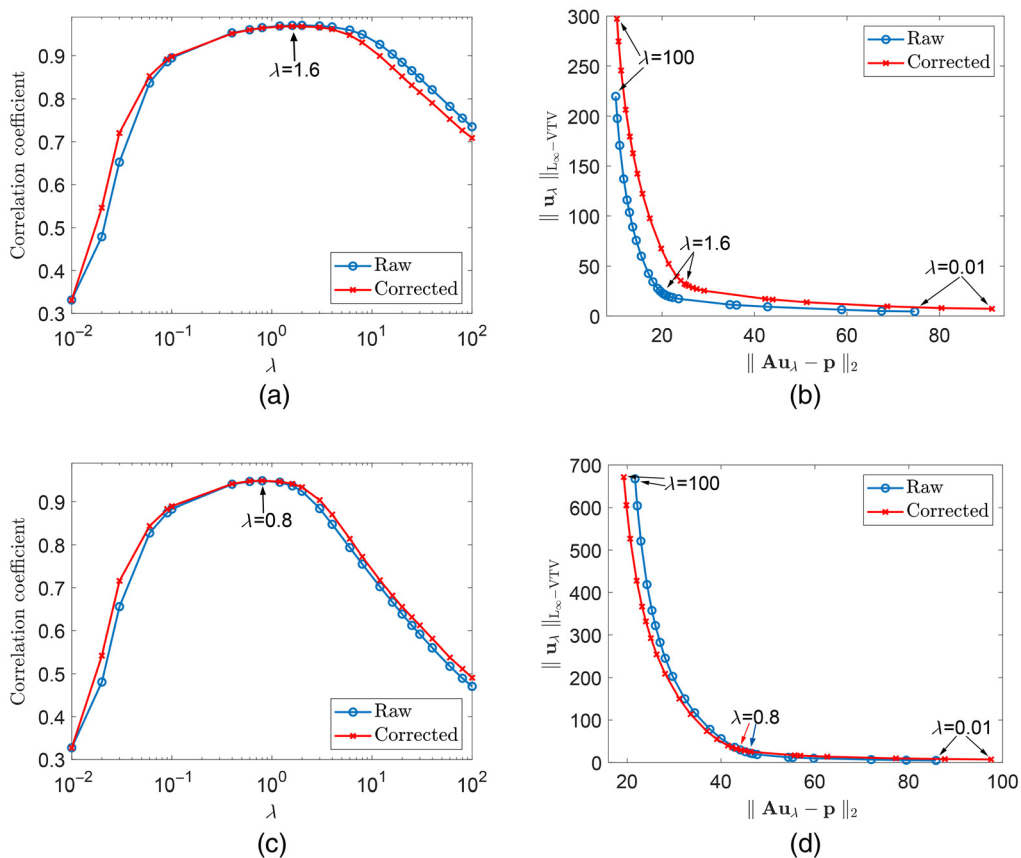


Fig. 7 Correlation coefficients as a function of weighting parameter λ (left column) and L-curves (right column) for the raw and corrected data, obtained from the integration times of (a), (b) 10 ms and (c), (d) 2 ms. The sample shown in Fig. 1(d) was employed to reproduce these results. The correlation coefficients represent the mean values calculated from the coefficients for 15 energy bins used. Note the logarithmic scale in the x-axis for correlation coefficients.

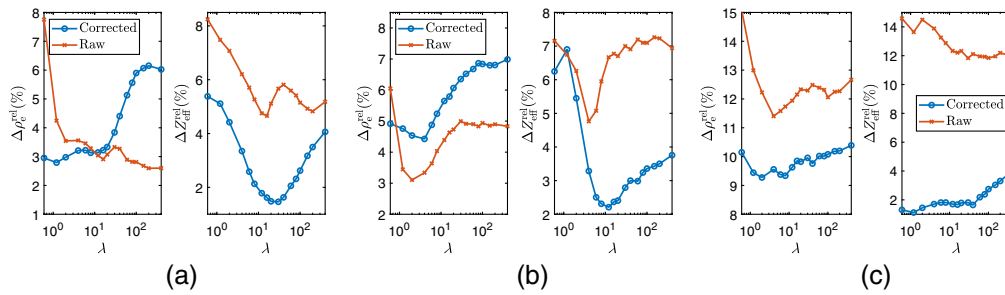


Fig. 8 The relative deviations as a function of weighting parameter λ for ρ_e and Z_{eff} , obtained with different integration times of (a) 100 ms, (b) 10 ms, and (c) 2 ms. The graphs show the mean absolute values of relative deviations for each material within the sample illustrated in Fig. 1(d). Note the logarithmic scale in the x-axis.

Table 4 The estimation of the material’s features from the raw and corrected data for different integration times, corresponding to the optimal λ values. The results from the whole range of λ are presented in Fig. 8.

Integration time (ms)	Raw			Corrected		
	λ	$\Delta\rho_e^{\text{rel}}$ (%)	$\Delta Z_{\text{eff}}^{\text{rel}}$ (%)	λ	$\Delta\rho_e^{\text{rel}}$ (%)	$\Delta Z_{\text{eff}}^{\text{rel}}$ (%)
100	200	2.6	4.8	16	3.2	1.6
10	4	3.3	4.8	6	4.9	2.5
2	100	12.1	11.8	1.2	9.4	1.1

and the value giving the maximum correlation coefficient. It can be seen from the plots that both the raw and corrected data in the case of 2 ms yield L-curves with less sharp corners compared to those obtained using 10 ms. However, the raw data present slightly less deflection of the curve from the vertical position than the corrected data.

Figure 8 presents the relative deviations for ρ_e and Z_{eff} as a function of λ , obtained with the total integration times per projection: 100, 10, and 2 ms. The calibration parameters used for (ρ_e , Z_{eff}) calculation were computed using the reference materials listed in Table 1. Table 4 tabulates the deviations corresponding to the optimal λ values. The corrected data have significantly higher accuracy of Z_{eff} estimation than the raw data for all the integration times. When the integration time is equal to 2 ms, the raw data result in deviations higher than 11% for both Z_{eff} and ρ_e , while the corrected data yield deviations higher than 9% for ρ_e and lower than 2% for Z_{eff} . The corrected data show that even though the deviations in Z_{eff} estimation for 2 ms appear to be lower than those for 10 ms, the former case with increased deviations in ρ_e estimation gives lower overall classification performance than the latter, as expected. Moreover, the corrected data exhibit more stable deviations over the range of λ values than the raw data for all the integration times. Thus, the correction algorithm can significantly increase the accuracy of Z_{eff} estimation and provide better robustness when the radiation dose levels are low.

5.4 Artificial Noise in Specific Energy Bins

The aim of the joint reconstruction is to correlate intensity shifts across the spectral dimensions such that noise in one energy bin blurring a specific edge is corrected by the information in the other bins of the same edge. Note that the term “edges” refers to sharp discontinuities separating different homogeneous regions in the image reconstruction. The joint reconstruction encourages the images in multiple energy bins to more efficiently preserve the edges. The correction algorithm redistributes intensity between energy bins based on the detector response and noise in one

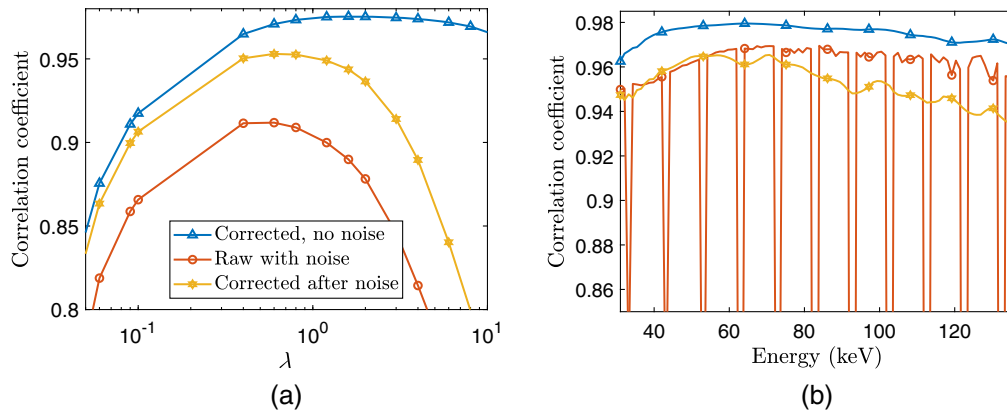


Fig. 10 Correlation coefficient as a function of (a) weighting parameter λ and (b) the photon energy between the low and high energy thresholds, obtained from the different noise cases introduced in Fig. 9. The correlation coefficients in the left frame represent the mean values calculated from the coefficients for the 96 energy bins. For each noise case, the correlation coefficient in the right frame corresponds to the optimal λ that gives the maximal correlation coefficient presented in the left frame. The sample shown in Fig. 1(d) was used to obtain these results. Note the logarithmic scale of the x-axis for correlation coefficients in the left frame.

bin is thus distributed across the spectrum. We aimed to check the robustness of the combined workflow of spectral correction and reconstruction to this type of noise in certain energies. Therefore, Gaussian noise with a standard deviation (σ) of 1.5 was introduced to the 11 energy bins distributed uniformly between 33.2 and 132.2 keV. The sample used in this section is demonstrated in Fig. 1(d). This sample was scanned with the total integration time per projection of 100 ms. We investigated three different cases: the raw data are corrected without adding noise (corrected, no noise), noise is added to the raw data and the resulting data are not corrected (raw with noise), and noise is added to the raw data and then the resulting data are corrected (corrected after noise). Figure 9 shows energy-resolved LACs extracted from an aluminum segment for each case. The correction algorithm appears to largely overcome such unexpected high noise except it shows some decrease in spectral LAC at low energies.

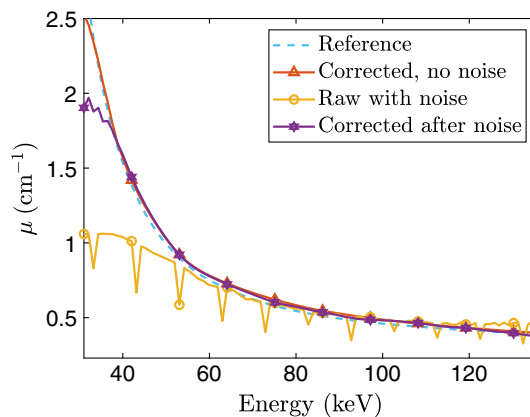


Fig. 9 Spectral LAC for aluminum obtained with three different noise cases after Gaussian noise with $\sigma = 1.5$ was added to 11 energy bins evenly distributed between the low and high energy thresholds; in case 1 the data are corrected without adding the noise, in case 2 the noise is added to the raw data and the resulting noisy data are not corrected, and in case 3 the noise is added to the raw data and the resulting noisy data are corrected. The reference LACs were obtained from NIST cross-sections.⁶⁷ The spectral LACs for each noise case were reconstructed with the optimal λ that gives the maximal correlation coefficient presented in Fig. 10(a). The sample shown in Fig. 1(d) was used to obtain these results.

Figure 10(a) presents correlation coefficients r for the above cases as a function of λ . The correction without adding noise gives $r = 0.97$ (at $\lambda = 1.6$). The noisy raw data without the correction give $r = 0.91$ (at $\lambda = 0.6$), whereas the correction of the noisy raw data gives $r = 0.95$ (at $\lambda = 0.6$). When the noise is added to the raw data in both cases, the reconstruction algorithm uses lower λ values to impose more regularization. Figure 10(b) shows correlation coefficients r for these cases as a function of photon energy. The correction after adding such noise significantly compensates for the affected energy bins with the noise, however, the correlation coefficients become lower compared with those in the case when the correction is applied to the raw data without added noise. The affected bins are clearly visible with sharp drops in the correlation coefficients when the raw data with the noise are not corrected. Thus, the robustness to such noise levels shows the significance of the correction and joint reconstruction, as it gives a noticeable reconstruction quality enhancement.

6 Conclusion

We have explored the influence of spectral distortion correction of a PCD on energy-resolved LACs, the correlation coefficient, and the L-curve criterion, and more importantly on material classification, using experimental data acquired with laboratory spectral CT. The correction algorithm corrects for the spectral distortions in the measured flat-field and attenuated x-ray spectra based on semianalytical models of the various detector effects, and thereby largely recovers the original spectrum. The classification performance with and without the spectral correction was estimated through system-independent material properties such as ρ_e and Z_{eff} . For material classification, we investigated the influence of spectral correction both for high resolution spectral reconstruction where the number of bins exceeds the energy resolution of the detector and for computational efficient binning of the spectral dimension into the low- and high-energy bins. In both approaches, we found that the correction algorithm can significantly increase classification performance as it qualitatively enhances the low-energy part of the LAC with respect to theoretical values. The classification performances of the raw and corrected data have been tested on different numbers of projections and different integration times of the detector.

The correlation coefficient was employed to assess reconstruction quality. We have found that at low integration times reconstructions from raw and corrected data result in similar correlation coefficients and L-curve features. Noise introduced to certain energy bins deteriorates reconstruction quality more for raw data than for data corrected after the noise is added. The correction algorithm thus shows robustness to noise in specific energy bins in terms of correcting the detector response. We show that classification relies on an accurate and reproducible attenuation signature and a high quality of classification is useful for medical applications to differentiate tissues with little contrast separation and security applications where restricted materials closely resemble common luggage items. Since the spectral correction of the detector response could easily be implemented for other types of photon counting detectors, results similar to what is obtained in this study can be expected when the correction algorithm is used for other photon-counting applications and set-ups.

Disclosures

No conflicts of interest are declared by the authors.

Acknowledgments

This project has received funding from the European Union Horizon 2020 research and innovation programme under the Marie Skłodowska-Curie Grant Agreement No. 765604 as part of the MULTIscale, Multimodal, and Multidimensional imaging for EngineeRING project⁷⁸ and from the EIC FTI program (project 853720). The authors want to acknowledge also the 3D Imaging Center at DTU, where the experiments have been conducted. Preliminary results of this work have been presented at the SPIE Optics + Optoelectronics Conference on Quantum Optics and Photon Counting (2021) and published in the conference proceedings.⁷⁹

Data and Code Availability

The raw and corrected data used to achieve the presented results are available to download from Ref. 80. Our implementation of the code for L_{∞} -VTV joint reconstruction algorithm is available at <https://github.com/JuliaTomo/XfromProjections.jl>.

References

1. Z. Qi et al., "Quantitative imaging of electron density and effective atomic number using phase contrast CT," *Phys. Med. Biol.* **55**(9), 2669–2677 (2010).
2. M. D. Agrawal et al., "Oncologic applications of dual-energy CT in the abdomen," *Radiographics* **34**(3), 589–612 (2014).
3. H. W. Goo and J. M. Goo, "Dual-energy CT: new horizon in medical imaging," *Korean J. Radiol.* **18**(4), 555–569 (2017).
4. M. Antoniassi, A. L. Conceição, and M. E. Poletti, "Study of effective atomic number of breast tissues determined using the elastic to inelastic scattering ratio," *Nucl. Instrum. Methods Phys. Res. A* **652**(1), 739–743 (2011).
5. M. Bazalova and E. E. Graves, "The importance of tissue segmentation for dose calculations for kilovoltage radiation therapy," *Med. Phys.* **38**(6), 3039–3049 (2011).
6. M. Kurudirek, "Effective atomic numbers and electron densities of some human tissues and dosimetric materials for mean energies of various radiation sources relevant to radiotherapy and medical applications," *Radiation Phys. Chem.* **102**, 139–146 (2014).
7. H. Manjunatha, "Comparison of effective atomic numbers of the cancerous and normal kidney tissue," *Radiation Prot. Environ.* **38**(3), 83 (2015).
8. H. C. Manjunatha and L. Seenappa, "Pocket formula for mass attenuation coefficient, effective atomic number, and electron density of human tissues," *Nucl. Sci. Tech.* **30**(3) (2019).
9. M. Ellenbogen and R. Bijjani, "Liquids and homemade explosive detection," *Proc. SPIE* **7306**, 73060Y (2009).
10. R. E. Alvarez and A. Macovski, "Energy-selective reconstructions in x-ray computerised tomography," *Phys. Med. Biol.* **21**(5), 733–744 (1976).
11. E. Kalender et al., "Evaluation of a prototype dual-energy computed tomographic apparatus. I. Phantom studies," *Med. Phys.* **13**(3), 334–339 (1986).
12. B. J. Heismann, J. Leppert, and K. Stierstorfer, "Density and atomic number measurements with spectral x-ray attenuation method," *J. Appl. Phys.* **94**(3), 2073–2079 (2003).
13. Z. Ying, R. Naidu, and C. R. Crawford, "Dual energy computed tomography for explosive detection," *J. X-Ray Sci. Technol.* **14**(4), 235–256 (2006).
14. J. S. Park and J. K. Kim, "Calculation of effective atomic number and normal density using a source weighting method in a dual energy x-ray inspection system," *J. Korean Phys. Soc.* **59**(4), 2709–2713 (2011).
15. T. P. Szczykutowicz, Z. Qi, and G.-H. Chen, "A simple image based method for obtaining electron density and atomic number in dual energy CT," *Proc. SPIE* **7961**, 79613A (2011).
16. O. Semerci and E. L. Miller, "A parametric level-set approach to simultaneous object identification and background reconstruction for dual-energy computed tomography," *IEEE Trans. Image Process.* **21**(5), 2719–2734 (2012).
17. G. Landry et al., "Deriving effective atomic numbers from DECT based on a parameterization of the ratio of high and low linear attenuation coefficients," *Phys. Med. Biol.* **58**(19), 6851–6866 (2013).
18. H. E. Martz et al., *X-Ray Imaging: Fundamentals, Industrial Techniques and Applications*, CRC Press (2016).
19. S. Ohira et al., "Estimation of electron density, effective atomic number and stopping power ratio using dual-layer computed tomography for radiotherapy treatment planning," *Phys. Med.* **56**(September), 34–40 (2018).
20. G. J. Pelgrim et al., "Accuracy of iodine quantification using dual energy CT in latest generation dual source and dual layer CT," *Eur. Radiol.* **27**(9), 3904–3912 (2017).

21. K. Wells and D. A. Bradley, "A review of x-ray explosives detection techniques for checked baggage," *Appl. Radiat. Isotopes* **70**(8), 1729–1746 (2012).
22. P. M. Shikhaliev, "Energy-resolved computed tomography: first experimental results," *Phys. Med. Biol.* **53**(20), 5595–5613 (2008).
23. A. Brambilla et al., "CdTe linear pixel x-ray detector with enhanced spectrometric performance for high flux x-ray imaging," *IEEE Trans. Nucl. Sci.* **59**(4 PART 3), 1552–1558 (2012).
24. X. Wang et al., "Material separation in x-ray CT with energy resolved photon-counting detectors," *Med. Phys.* **38**(3), 1534–1546 (2011).
25. M. Joshi et al., "Effective atomic number accuracy for kidney stone characterization using spectral CT," *Proc. SPIE* **7622**, 76223K (2010).
26. K. Taguchi and J. S. Iwanczyk, "Vision 20/20: single photon counting x-ray detectors in medical imaging," *Med. Phys.* **40**(10), 100901 (2013).
27. N. G. Anderson and A. P. Butler, "Clinical applications of spectral molecular imaging: Potential and challenges," *Contrast Media Mol. Imaging* **9**(1), 3–12 (2014).
28. P. M. Shikhaliev, "Soft tissue imaging with photon counting spectroscopic CT," *Phys. Med. Biol.* **60**(6), 2453–2474 (2015).
29. C. P. A. Brambilla et al., "Basis material decomposition method for material discrimination with a new spectrometric x-ray imaging detector," *J. Instrum.* **12**(8), P08014 (2017).
30. L. Martin, "Enhanced information extraction in multi-energy x-ray tomography for security," PhD thesis, Boston University (2014).
31. M. Busi, "Enhanced security screening using spectral x-ray imaging," PhD thesis, Technical University of Denmark (2019).
32. M. J. Willemink et al., "Photon-counting CT: technical principles and clinical prospects," *Radiology* **289**(2), 293–312 (2018).
33. S. Leng et al., "Photon-counting detector CT: system design and clinical applications of an emerging technology," *Radiographics* **39**(3), 729–743 (2019).
34. M. Simard et al., "Quantitative imaging performance of MARS spectral photon-counting CT for radiotherapy," *Med. Phys.* **47**(8), 3423–3434 (2020).
35. M. Danielsson, M. Persson, and M. Sjölin, "Photon-counting x-ray detectors for CT," *Phys. Med. Biol.* **66**(3), 03TR01 (2021).
36. K. Taguchi, I. Blevins, and K. Iniewski, *Spectral, Photon Counting Computed Tomography: Technology and Applications*, CRC Press (2020).
37. F. K. Kopp et al., "Evaluation of a preclinical photon-counting CT prototype for pulmonary imaging," *Sci. Rep.* **8**, 17386 (2018).
38. M. Mannil et al., "Photon-counting CT: high-resolution imaging of coronary stents," *Invest. Radiol.* **53**(3), 143–149 (2018).
39. M. Sigovan et al., "Feasibility of improving vascular imaging in the presence of metallic stents using spectral photon counting CT and K-edge imaging," *Sci. Rep.* **9**(1), 1–9 (2019).
40. R. Symons et al., "Quarter-millimeter spectral coronary stent imaging with photon-counting CT: initial experience," *J. Cardiovasc. Comput. Tomogr.* **12**(6), 509–515 (2018).
41. R. Symons et al., "Photon-counting CT for vascular imaging of the head and neck: first *in vivo* human results," *Invest. Radiol.* **53**(3), 135 (2018).
42. V. Rebuffel et al., "New perspectives of x-ray techniques for explosive detection based on CdTe/CdZnTe spectrometric detectors," in *Proc. of the Int. Symp. on Digit. Ind. Radiol. and Comput. Tomogr.*, Vol. 2, pp. 1–8 (2011).
43. J. Rinkel et al., "Experimental evaluation of material identification methods with CdTe x-ray spectrometric detector," *IEEE Trans. Nucl. Sci.* **58**(5), 2371–2377 (2011).
44. G. Beldjoudi et al., "Multidimensional data processing methods for material discrimination using an ideal x-ray spectrometric photon counting detector," *IEEE Trans. Nucl. Sci.* **58**(6 PART 2), 3190–3203 (2011).
45. G. Beldjoudi et al., "An optimised method for material identification using a photon counting detector," *Nucl. Instrum. Methods Phys. Res. A* **663**(1), 26–36 (2012).
46. S. G. Azevedo et al., "System-independent characterization of materials using dual-energy computed tomography," *IEEE Trans. Nucl. Sci.* **63**(1), 341–350 (2016).

47. K. M. Champley et al., "Method to extract system-independent material properties from dual-energy x-ray CT," *IEEE Trans. Nucl. Sci.* **66**(3), 674–686 (2019).
48. M. Busi et al., "Method for system-independent material characterization from spectral x-ray CT," *NDT E Int.* **107**(August), 102136 (2019).
49. D. Jumanazarov et al., "System-independent material classification through x-ray attenuation decomposition from spectral x-ray CT," *NDT E Int.* **116**(July), 102336 (2020).
50. E. S. Dreier et al., "Spectral correction algorithm for multispectral CdTe x-ray detectors," *Opt. Eng.* **57**(5), 16 (2018).
51. A. H. Compton et al., *X-Rays in Theory and Experiment*, Vol. 82, Van Nostrand, New York, NY, USA (1935).
52. W. V. Mayneord, "The significance of the Roentgen," *Acta Int. Union Against Cancer* **2**, 271 (1937).
53. F. W. Spiers, "Effective atomic number and energy absorption in tissues," *Br. J. Radiol.* **19**(218), 52–63 (1946).
54. J. Gregor and T. Benson, "Computational analysis and improvement of SIRT," *IEEE Trans. Med. Imaging* **27**(7), 918–924 (2008).
55. S. Kim et al., "PubChem 2019 update: improved access to chemical data," *Nucleic Acids Res.* **47**(D1), D1102–D1109 (2019).
56. Shivaramu, "Effective atomic numbers for photon energy absorption and photon attenuation of tissues from human organs," *Med. Dosimetry* **27**(1), 1–9 (2002).
57. M. A. Zenobio et al., "Effective atomic number of human enamel and dentin within a photon energy range from 10 to 200 KeV," (2011).
58. H. C. Manjunatha and B. Rudraswamy, "Study of effective atomic number and electron density for tissues from human organs in the energy range of 1 keV-100 GeV," *Health Phys.* **104**(2), 158–162 (2013).
59. T. Flohr et al., "Photon-counting CT review," *Phys. Med.* **79**(October), 126–136 (2020).
60. A. Brambilla et al., "Fast CdTe and CdZnTe semiconductor detector arrays for spectroscopic x-ray imaging," *IEEE Trans. Nucl. Sci.* **60**(1), 408–415 (2013).
61. M. Persson et al., "Energy-resolved CT imaging with a photon-counting silicon-strip detector," *Phys. Med. Biol.* **59**(22), 6709–6727 (2014).
62. Y. Eisen and Y. Horovitz, "Correction of incomplete charge collection in CdTe detectors," *Nucl. Instrum. Methods Phys. Res. A* **353**(1–3), 60–66 (1994).
63. D. S. McGregor and H. Hermon, "Room-temperature compound semiconductor radiation detectors," *Nucl. Instrum. Methods Phys. Res. A* **395**(1), 101–124 (1997).
64. H. H. Barrett, J. Eskin, and H. Barber, "Charge transport in arrays of semiconductor gamma-ray detectors," *Phys. Rev. Lett.* **75**(1), 156 (1995).
65. H. Toyama et al., "Quantitative analysis of polarization phenomena in CdTe radiation detectors," *Jpn. J. Appl. Phys.* **45**(11), 8842–8847 (2006).
66. D. S. Bale and C. Szeles, "Nature of polarization in wide-bandgap semiconductor detectors under high-flux irradiation: application to semi-insulating $\text{Cd}_{1-x}\text{Zn}_x\text{Te}$," *Phys. Rev. B – Condens. Matter Mater. Phys.* **77**(3), 1–16 (2008).
67. K. Berger et al., *XCOM: Photon Cross Section Database*, National Institute of Standards and Technology (NIST), Gaithersburg, Maryland (2010).
68. P. Guerra, A. Santos, and D. G. Darambara, "Development of a simplified simulation model for performance characterization of a pixellated CdZnTe multimodality imaging system," *Phys. Med. Biol.* **53**(4), 1099–1113 (2008).
69. J. Plagnard, "Comparison of measured and calculated spectra emitted by the x-ray tube used at the Gustave Roussy radiobiological service," *X-Ray Spectr.* **43**(5), 298–304 (2014).
70. D. Jumanazarov et al., "Material classification from sparse spectral x-ray CT using vectorial total variation based on L infinity norm [data set]," *Mater. Charact.* **187**, 111864 (2022).
71. A. S. Wang and N. J. Pelc, "Optimal energy thresholds and weights for separating materials using photon counting x-ray detectors with energy discriminating capabilities," *Proc. SPIE* **7258**, 725821 (2009).
72. A. S. Wang and N. J. Pelc, "Sufficient statistics as a generalization of binning in spectral x-ray imaging," *IEEE Trans. Med. Imaging* **30**(1), 84–93 (2011).

73. P. C. Hansen, "The L-curve and its use in the numerical treatment of inverse problems," in *Computational Inverse Problems in Electrocardiology*, P. Johnston, Ed., Advances in Computational Bioengineering, Vol. 4, pp. 119–142, WIT Press (2000).
74. X. Yang et al., "TV-based conjugate gradient method and discrete L-curve for few-view CT reconstruction of x-ray *in vivo* data," *Opt. Express* **23**(5), 5368 (2015).
75. J. Nocedal and S. J. Wright, *Numerical Optimization*, Springer, New York (1999).
76. A. E. Papadakis and J. Damilakis, "Fast kVp-switching dual energy contrast-enhanced thorax and cardiac CT: a phantom study on the accuracy of iodine concentration and effective atomic number measurement," *Med. Phys.* **44**(9), 4724–4735 (2017).
77. D. Kawahara et al., "Accuracy of the raw-data-based effective atomic numbers and monochromatic CT numbers for contrast medium with a dual-energy CT technique," *Br. J. Radiol.* **91**(1082), 20170524 (2018).
78. MUMMERING, "Innovative training network," www.mumming.eu.
79. D. Jumanazarov et al., "The significance of the spectral correction of photon counting detector response in material classification from spectral x-ray CT," *Proc. SPIE* **11771**, 60–76 (2021).
80. D. Jumanazarov et al., "Material classification from sparse spectral x-ray 803 CT using vectorial total variation based on L infinity norm [data set]," Zenodo (2021).

Doniyor Jumanazarov has recently received his PhD from the Department of Physics at Denmark Technical University (DTU), Kongens Lyngby, Denmark. He received his BS degree in physics from the National University of Uzbekistan, Tashkent, Uzbekistan, and his MS degree in molecular photonics for bio- and nanotechnologies (MONABIPHOT) from the École Normale Supérieure de Cachan, Cachan, France, in 2012 and 2018, respectively.

Jakeoung Koo received his BSc and MSc degrees in computer science from Chung-Ang University, South Korea, in 2015 and 2017, respectively. He has received his PhD from DTU, Kongens Lyngby, Denmark. His research interests lie in computed tomography and computer vision.

Henning F. Poulsen is employed at DTU Physics since 2012. He pioneered several x-ray microscopy methods enabling multiscale mapping of materials properties from the macroscopic and down to nanometer length scales. He heads the 3D Imaging Centre at DTU and is a principal investigator on a number of European and national projects with the aim of introducing x-ray methods to industry.

Ulrik L. Olsen has been a senior research engineer at DTU Physics since 2013. He received his PhD in 2009 from Copenhagen University. He is an expert in x-ray instrumentation and specialises in spectral x-ray detectors, data acquisition, and processing. His current research interest is the use of spectral detectors for security applications for improved reconstruction and material identification.

Mihai Iovea, engineer in physics, senior research scientist, PhD in physics, has over 30 years' experience in x-ray imaging projects research and development for security and non-destructive testing. He is interested in x-ray 2D and 3D tomography and digital radiography techniques, such as dual/multienergy, diffraction, backscattering applied in for threats detection, high-resolution in-line x-ray scanners for fast, nondestructive industrial testing.